First-Principles Calculations to Investigate Structural, Electronic, Optical and Magnetic Properties of Pyrochlore Oxides Eu$_2$Tm$_2$O$_7$ (Tm = Hf, Sn, Zr) for Energy Applications

Zeesham Abbas [1], Adeela Naz [2], Sajjad Hussain [1], Shabbir Muhammad [3], H. Algarni [4], Ahsan Ali [5,*] and Jongwan Jung [1,*]

1 Department of Nanotechnology and Advanced Materials Engineering, Sejong University, Seoul 05006, Republic of Korea; zeesham_66@yahoo.com (Z.A.)
2 Department of Physics, The University of Lahore, Sargodha Campus, Sargodha 40100, Pakistan
3 Department of Chemistry, College of Science, King Khalid University, P.O. Box 9004, Abha 61413, Saudi Arabia
4 Department of Physics, College of Science, King Khalid University, P.O. Box 9004, Abha 61413, Saudi Arabia
5 Department of Mechanical Engineering, Gachon University, Seongnam 13120, Republic of Korea
* Correspondence: ahsanali@gachon.ac.kr (A.A.); jwjung@sejong.ac.kr (J.J.)

Abstract: Three newly designed pyrochlore oxides, Eu$_2$Tm$_2$O$_7$ (Tm = Hf, Sn, Zr), are analyzed for their magnetic, optical and electronic properties using ab-initio calculations within the context of density functional theory (DFT). We can refer these compounds as direct bandgap materials because there is a very slight difference between the height of bands at the Γ- and M-point. It is observed that bandgap engineering can be performed by replacing Hf with Sn and Zr. It is observed from total density of states (TDOS) plots that shape and height of curves is not the same in spin up and spin down channels, showing significant magnetic moment in these compounds. It is evident from magnetic properties that a major portion of total magnetic moment (m_{tot}) comes from Eu-atoms. In all compounds, the magnetic moment of O, Hf, Sn and Zr atoms is negative, whereas the magnetic moment of Eu-atoms is positive, showing their antiparallel arrangement. In both spin channels, significant absorption of the incoming photons is also shown by these compounds in the ultraviolet (UV) region. We can conclude on the basis of $R(\omega)$ that these compounds can be utilized in applications such as anti-reflecting coatings. These compounds are potential candidates for photovoltaic applications, such as solar cells, due to efficient absorption of incoming photons in visible and UV regions.

Keywords: pyrochlore oxides; optoelectronic properties; magnetic properties; DFT; first-principles; solar cell

1. Introduction

Pyrochlore oxides with the general formal A$_2$B$_2$O$_7$ have attracted huge attention from scientists due to their interesting thermal, piezoelectric, ferroelectric and dielectric properties since their first discovery in the early 1960s [1–3]. Pyrochlores are promising candidates for broad applications in technological [4–8] and industrial fields such as luminescence powders [9,10], probes and sensors [11–13], thermal barrier coatings [14,15] and solid oxide fuel cells [16]. Generally, pyrochlore oxides of the A$_2$B$_2$O$_7$ type crystallize into FCC (face centered cubic) crystals with the space group $Fd\overline{3}m$ (S. G. # 227). In ideal pyrochlore structures, rare earth element and transition metal occupies the A-site (16d) and B-site (16c), respectively. The anions take 8b and 48f Wyckoff positions to form an ordered structure. The large and small size cations are placed at the A- and B-site, respectively, in the crystal unit cell. The cation at the A- (positioned within a distorted polyhedron) and B-site (positioned within a distorted octahedron) are 8- and 6-fold coordinated with oxygen atoms, respectively [17,18]. The structural stability of pyrochlore oxides of the A$_2$B$_2$O$_7$ type

is significantly influenced by the ionic radius of the A- and B-site cations. In these type of pyrochlores, the stable and suitable ordered cubic phase exists when the radii ratio of A- and B-site cations (r_A/r_B) are between 1.46 and 1.78. The crystal geometry transforms to monoclinic from the cubic phase when this value (r_A/r_B) is greater than 1.78. On the other hand, a disordered (anion deficient fluorite structure) structure is formed, which conforms with the $Fm\overline{3}m$ space group. In defective fluorite structures, A- and B-site ions are randomly distributed at the 4a (cation sites) Wyckoff position, and the oxygen vacancies are disordered at 8c (anion sites) Wyckoff positions [19,20]. In addition, this temperature- and pressure-influenced phase transformation can significantly affect physical properties (such as conductivity and compressibility) of the crystal [21,22].

Augilar et al. [23] reported that the efficiency of solar cells can be enhanced by using a mixture of $Tm_2Ti_2O_7$ and TiO_2 for the photoelectrode while studying $Tm_2Ti_2O_7$ for the dye-sensitized solar cells. N. Ullah et al. [24] reported that $Y_2M_2O_7$ (M = Ti, V and Nb) pyrochlores are semiconducting compounds with excellent optical properties while studying their optical and electronic properties. Magnetic properties of platinum base pyrochlore oxides are also reported in the literature [25,26]. For industrial applications (such as thermoelectric and photovoltaic devices), developing suitable materials is the primary goal of researchers in the field of renewable energy. Exceptional chemical and physical properties are a prerequisite for these materials. For catalysis and electrochemistry, Re-X-O ternary systems exhibit numerous desired properties. Here, Re and X are used for rare earth elements and platinum group metals, respectively [27]. For phase equilibrium and thermodynamic properties, various ternary Re-X-O have extensively been investigated at high temperatures [28]. For numerous technological applications, $La_2Pd_2O_7$ is a promising candidate from this family [29]. $Ca_{1-x}Bi_xPd_3O_4$ (n-type semiconductor) and $Ca_{1-x}Li_xPd_3O_4$ (p-type semiconductor) are both fascinating candidates for thermoelectric applications. Their low mobility due to large effective mass is the primary obstacle for their usability in thermoelectric (TE) devices [30]. Attfield et. Al. [31] used a simple modeling technique along with powder diffraction to analyze crystalline structures of pyrochlores such as La_4PdO_7 and $La_2Pd_2O_5$. Various types of energy production methods are available in the literature [32,33].

Pyrochlore oxides are effective photon absorbers as well as promising candidates for TE device applications due to appropriate TE characteristics. In this study, electronic, optical and magnetic properties of $Eu_2Tm_2O_7$ (Tm = Hf, Sn, Zr) are investigated using first-principles-based DFT calculations. Ground state properties (electronic, optical and magnetic) of $Eu_2Tm_2O_7$ (Tm = Hf, Sn, Zr) are studied using the full-potential linearized augmented plane wave (FP-LAPW) method to obtain an insight of their prospective applications in photovoltaic, spintronic and TE devices. The DFT technique is used to calculate optoelectronic, structural and magnetic properties of $Eu_2Tm_2O_7$ (Tm = Hf, Sn, Zr) to evaluate their potential for various industrial applications such as solar cells and memory devices.

2. Results and Discussion

In this section, we discuss the investigated results for electronic, optical and magnetic properties of $Eu_2Tm_2O_7$ (Tm = Hf, Sn, Zr). Their potential for clean energy production using photovoltaic devices has been explored. For optoelectronic applications, usability of these pyrochlore oxides was investigated using their optoelectronic characteristics. The magnetic properties are key parameters to explore the potential of $Eu_2Tm_2O_7$ (Tm = Hf, Sn, Zr) for spintronic applications such as memory devices. Based on the presented results, it is established that $Eu_2Tm_2O_7$ (Tm = Hf, Sn, Zr) has huge potential for spintronic and optoelectronic devices.

2.1. Electronic Properties

In this section, we discuss the investigated electronic properties (density of states (DOS)/band structure) for $Eu_2Tm_2O_7$ (Tm = Hf, Sn, Zr). The role of various inter-

band/intra-band electronic transitions is important to determine the adequacy of $Eu_2Tm_2O_7$ (Tm = Hf, Sn, Zr) for prospective optoelectronic devices. In the first Brillouin zone, high symmetry points were used to present energy band structures (from −3.0 to 5.0 eV) with the Fermi level (E_g) at 0 eV. An energy range of −6.0 and 6.0 eV was used to present DOS spectra that give vital information regarding the feasible transitions between valance/conduction bands.

2.1.1. Energy Band Structure

For solid materials, the allowed and forbidden electronic energy levels are represented by band structures. In crystalline materials, the energies of the crystal orbitals are presented using 2D band structures. A band structure plot, sometimes called a "spaghetti diagram", can quickly reveal the nature of materials such as insulating, semi-metallic or metallic. The nature of the energy bandgap (direct or indirect) for semiconductor materials as well as magnitude of the bandgap can also be established using band structure plots. The difference of the energies of valance band maxima (VBM) and conduction band minima (CBM) is known as the energy bandgap. Moreover, the carrier mobility can also be determined using the curvature of these bands. Energy band structures for $Eu_2Tm_2O_7$ (Tm = Hf, Sn, Zr) are calculated along high symmetry points R→Γ→X→M→Γ. The calculated band structure plots for $Eu_2Tm_2O_7$ (Tm = Hf, Sn, Zr) are presented in Figure 1. We can refer to these compounds as direct bandgap materials because there is very slight difference between the height of bands at the Γ- and M-point. The values of energy bandgaps for $Eu_2Hf_2O_7$, $Eu_2Sn_2O_7$ and $Eu_2Zr_2O_7$ were 1.78, 1.85 and 1.80 eV, respectively, in the spin up channel. However, in the spin down channel, the values of energy bandgaps were 4.02, 2.42 and 3.98 eV for $Eu_2Hf_2O_7$, $Eu_2Sn_2O_7$ and $Eu_2Zr_2O_7$, respectively. It was observed that bandgap engineering could be performed by replacing Hf with Sn and Zr.
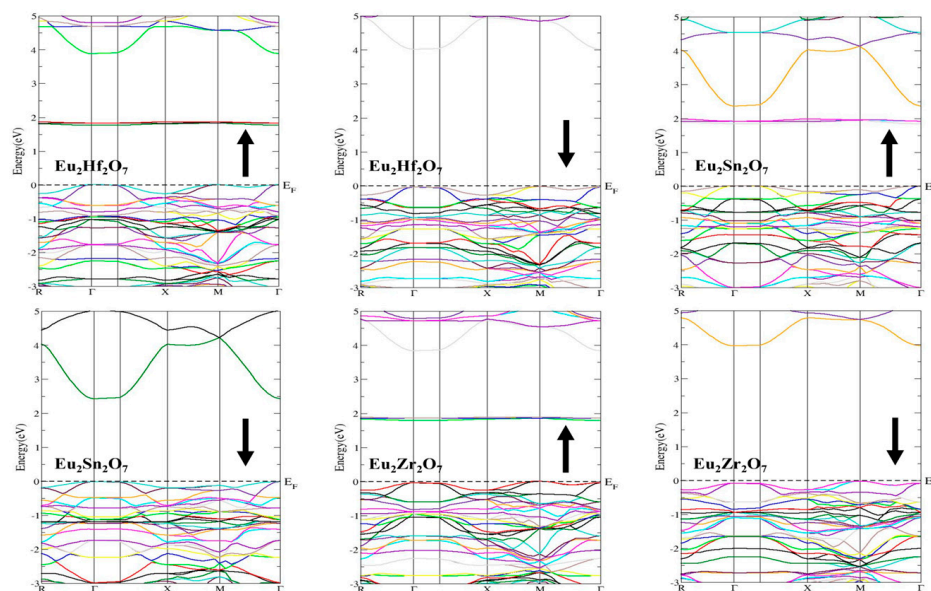
Figure 1. Calculated band structure plots for $Eu_2Tm_2O_7$ (Tm = Hf, Sn, Zr).

2.1.2. Density of States

The number of various energy states that electrons can occupy at a specific energy level, or the number of electronic states per unit volume per unit energy, are known as the density of states (DOS). This function defines bulk properties of conductive solids such as paramagnetic susceptibility, specific heat and other transport phenomena. In semiconductors, energy band spacing can be determined using DOS calculations, as well as the general distribution of states as a function of energy. The calculated total density of states (TDOS) plots for $Eu_2Tm_2O_7$ (Tm = Hf, Sn, Zr) are presented in Figure 2. We can

note from TDOS plots that the shape and height of curves are not the same in spin up and spin down channels, showing significant magnetic moment in these compounds. It can be noted that TDOS of $Eu_2Hf_2O_7$ are greater compared to $Eu_2Sn_2O_7$ and $Eu_2Zr_2O_7$, which means that $Eu_2Hf_2O_7$ has a greater probability for electronic transitions between valance and conduction bands.
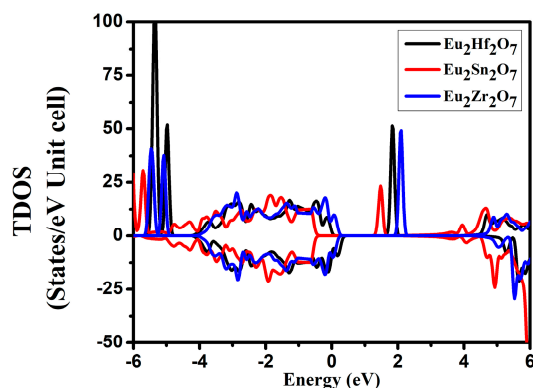
Figure 2. Calculated TDOS plots for $Eu_2Tm_2O_7$ (Tm = Hf, Sn, Zr).

The partial density of states gives information about the most probable electronic transitions between VB and CB from various sub-orbitals of the atoms. The calculated partial density of states (PDOS) plots for $Eu_2Hf_2O_7$ are presented in Figure 3. We can split the valance band of $Eu_2Hf_2O_7$ into two segments: (i) −6.0 to −4.0 eV and (ii) −4.0 to 0 eV. In segment (i), all compounds were approximately silent in the spin down channel; however, significant contributions in the spin up channel from Eu-atoms are evident from Figure 3. From PDOS plots, significant contributions from $Eu[4f^7]$ orbitals are evident in the spin up channel, along with minor contributions from $O[2p^4]$ orbitals. In segment (ii), O-atoms were actively participating in VB, whereas minor contributions from Hf-atoms are evident in both spin channels from Figure 3. From PDOS plots, significant contributions from $O[2p^4]$ and $Hf[5d^2]$ orbitals are evident in both spin channels, along with minor contributions from $Hf[5p^6]$ and $Hf[4f^{14}]$ orbitals. After that, there is a forbidden region for electrons known as the energy bandgap until 1.78 eV in the spin up channel and 4.02 eV in the spin down channel. A notable peak at 1.78 eV due to the hybridization of O, Eu and Hf-atoms was present in the spin up channel. In this peak, major contributions came from $Eu[4f^7]$ orbitals, along with minor contributions from $O[2p^4]$ and $Hf[5d^2]$ orbitals.
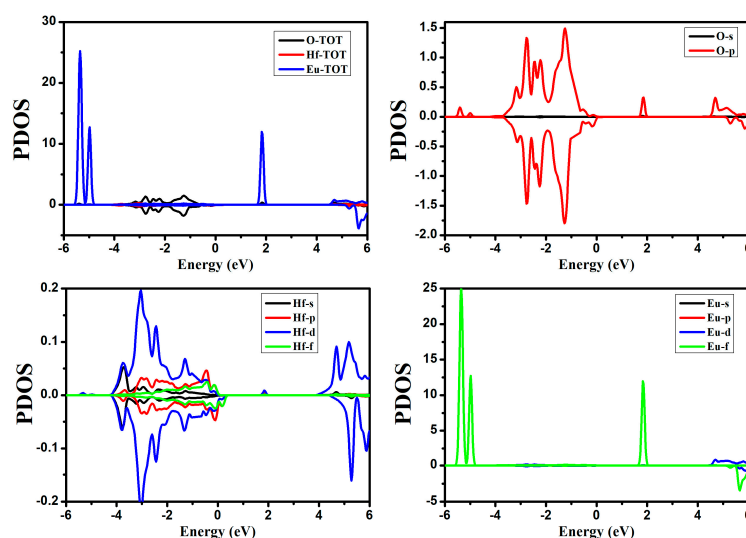
Figure 3. Calculated PDOS plots for $Eu_2Hf_2O_7$.

The calculated PDOS plots for $Eu_2Sn_2O_7$ are presented in Figure 4. We can split the valance band of $Eu_2Sn_2O_7$ into two segments: (i) -6.0 to -4.0 eV and (ii) -4.0 to 0 eV. In segment (i), all compounds were approximately silent in the spin down channel; however, significant contributions in the spin up channel from Eu-atoms are evident from Figure 4, along with minor contributions from Sn-atoms. From PDOS plots, significant contributions from $Eu[4f^7]$ orbitals are evident in the spin up channel, along with minor contributions from $Sn[5s^2]$ orbitals. In segment (ii), O-atoms were actively participating in VB, whereas minor contributions from Sn-atoms are evident in both spin channels from Figure 4. From PDOS plots, significant contributions from $O[2p^4]$ and $Sn[5p^2]$ orbitals are evident in both spin channels, along with minor contributions from $Sn[4d^{10}]$ orbitals. After that, there is a forbidden region for electrons known as the energy bandgap until 1.85 eV in the spin up channel and 4.42 eV in the spin down channel. A notable peak at 1.85 eV due to the hybridization of O and Eu-atoms was present in the spin up channel. In this peak, major contributions came from $Eu[4f^7]$ orbitals, along with minor contributions from $O[2p^4]$ orbitals.
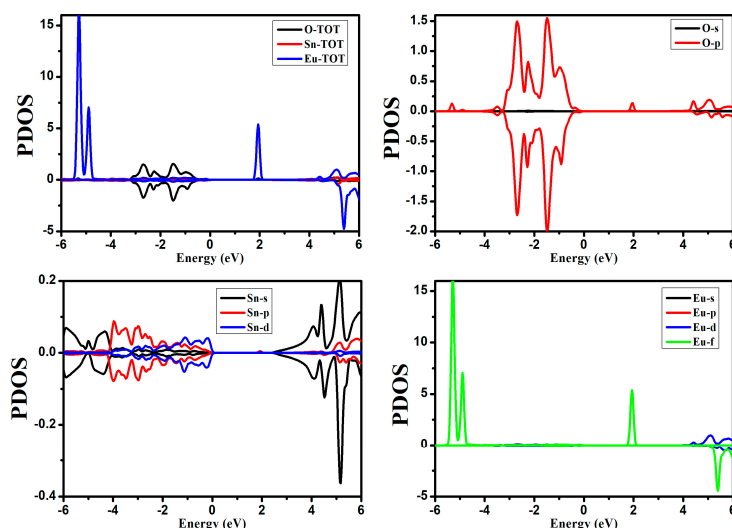
Figure 4. Calculated PDOS plots for $Eu_2Sn_2O_7$.

The calculated PDOS plots for $Eu_2Zr_2O_7$ are presented in Figure 5. We can split the valance band of $Eu_2Zr_2O_7$ into two segments: (i) -6.0 to -4.0 eV and (ii) -4.0 to 0 eV. In segment (i), all compounds were approximately silent in the spin down channel; however, significant contributions in the spin up channel from Eu-atoms are evident from Figure 5. From PDOS plots, significant contributions from $Eu[4f^7]$ orbitals are evident in the spin up channel, along with minor contributions from $O[2p^4]$ orbitals. In segment (ii), O-atoms were actively participating in VB, whereas minor contributions from Zr-atoms are evident in both spin channels from Figure 5. From PDOS plots, significant contributions from $O[2p^4]$ and $Zr[4d^2]$ orbitals are evident in both spin channels, along with minor contributions from $Zr[4p^6]$ orbitals. After that, there is a forbidden region for electrons known as the energy bandgap until 1.80 eV in the spin up channel and 3.98 eV in the spin down channel. A notable peak at 1.80 eV due to the hybridization of O, Eu and Zr-atoms was present in the spin up channel. In this peak, major contributions came from $Eu[4f^7]$ orbitals, along with minor contributions from $O[2p^4]$ and $Zr[4d^2]$ orbitals.
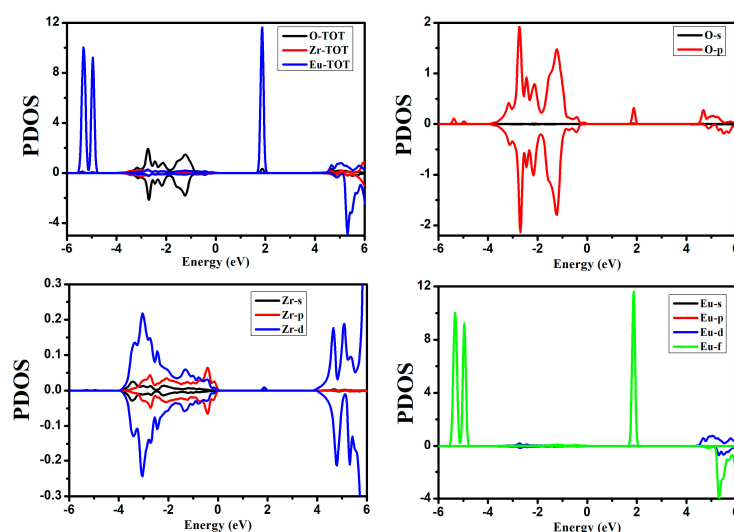
Figure 5. Calculated PDOS plots for $Eu_2Zr_2O_7$.

2.2. Magnetic Properties

In this section, we discuss the calculated magnetic properties for $Eu_2Tm_2O_7$ (Tm = Hf, Sn, Zr) to obtain an insight of prospective spintronic applications such as memory devices. The magnetic moment in $Eu_2Tm_2O_7$ (Tm = Hf, Sn, Zr) derives from the notable anisotropy present in occupied electronic states in spin up and spin down channels. In Table 1, we present calculated values of total/partial magnetic moments for aforesaid compounds. It is evident from Table 1 that a major portion of total magnetic moment (m_{tot}) comes from Eu-atoms. All compounds have nearly equal values of total magnetic moments. In all compounds, the magnetic moment of O, Hf, Sn and Zr atoms is negative, whereas the magnetic moment of Eu-atoms is positive, showing their antiparallel arrangement. Therefore, $Eu_2Tm_2O_7$ (Tm = Hf, Sn, Zr) are promising candidates for prospective spintronic applications.

Table 1. The calculated magnetic moments for $Eu_2Tm_2O_7$ (Tm = Hf, Sn, Zr).

Compound	Magnetic Moment (μ_B)				
$Eu_2Hf_2O_7$	m_{int} 0.31875	m_O −0.37218	m_{Hf} −0.00304	m_{Eu} 24.05657	m_{tot} 24.00011
$Eu_2Sn_2O_7$	m_{int} 0.33198	m_O −0.38122	m_{Sn} −0.00204	m_{Eu} 24.04723	m_{tot} 24.00003
$Eu_2Zr_2O_7$	m_{int} 0.32337	m_O −0.3775	m_{Zr} −0.00344	m_{Eu} 24.05768	m_{tot} 24.00012

2.3. Optical Properties

In this section, we have discuss the investigated optical characteristics for $Eu_2Tm_2O_7$ (Tm = Hf, Sn, Zr) to obtain an insight of the prospective optoelectronic applications such as solar cells. For targeted materials, results obtained from band structure calculations can be used to calculate their optical properties. To examine how a material responds to incident radiation, it is crucial to analyze its optical characteristics. Electronic transitions between the unoccupied and occupied states are the result of interactions between electric field and photons. Frequency-dependent complex dielectric function $\varepsilon(\omega)$ is the basic linear optical parameter that can be used to explain a crystal's response to the incident electromagnetic radiations. Equation (1) can be used to formulate $\varepsilon(\omega)$ [34].

$$\varepsilon(\omega) = \varepsilon_1(\omega) + i\varepsilon_2(\omega) \tag{1}$$

where $\varepsilon_1(\omega)$ and $\varepsilon_2(\omega)$ are, respectively, real and imaginary parts of the dielectric function. The electronic structure of crystalline materials can be explained using the most effective tool known as the optical absorption spectra. The real $\varepsilon_1(\omega)$ and imaginary $\varepsilon_2(\omega)$ part of dielectric function and other dependent parameters (on $\varepsilon_1(\omega)$ and $\varepsilon_2(\omega)$) are investigated theoretically using an equilibrium constant of 0–14 eV. Equation (1) can be used to formulate $\varepsilon_2(\omega)$:

$$\varepsilon_2(\omega) = \frac{Ve^2}{2\pi m^2 \omega^2} \int d^3k \sum_{n,n'} \langle k,n|p|k,n' \rangle^2 f(kn)[1-f(kn')]\delta(E_{kn}-E_{kn'}-\omega) \quad (2)$$

The first Brillouin zone is used to perform the integration in the above equation. The following dipole matrix elements are used to specify matrix elements for direct transitions between VB and CB:

$$M_{cv} = \langle u_{ck}|\delta.\nabla|u_{vk} \rangle \quad (3)$$

where vector potential of the electric field is represented by d. The imaginary part $\varepsilon_2(\omega)$ of the complex dielectric function and Kramer's Kroning relation (KKR) is used to formulate $\varepsilon_1(\omega)$ using Equation (4) [35]:

$$\varepsilon_1(\omega) = 1 + \frac{2}{\pi} \int_0^\infty \frac{\varepsilon_2(\omega)\omega' d\omega'}{\omega'^2 - \omega^2} \quad (4)$$

The calculated spectra of $\varepsilon_1(\omega)$ and $\varepsilon_2(\omega)$ for $Eu_2Tm_2O_7$ (Tm = Hf, Sn, Zr) using the GGA+U approximation are shown in the Figure 6. The major peaks around 6.0 eV in the spectra of $\varepsilon_1(\omega)$ after static values show that the maximum dispersion of the incoming photons by these materials occurs at this value. We can spot in the spectra of $\varepsilon_1(\omega)$ that the curves of $Eu_2Tm_2O_7$ (Tm = Hf, Sn, Zr) enter the negative region at approximately 10 eV. The materials show a metallic behavior in the negative region, and values at which the curves cross the zero energy axis is known as the plasmon frequency. Values of the $\varepsilon_1(\omega)$ at zero frequency ($\omega = 0$) are known as static values of the dielectric function $\varepsilon_1(0)$. The values of $\varepsilon_1(0)$ and E_g are inversely related with each other using Equation (5), known as Penn's model [36]:

$$\varepsilon_1(0) = 1 + \left(\frac{h\omega_p}{E_g}\right) \quad (5)$$
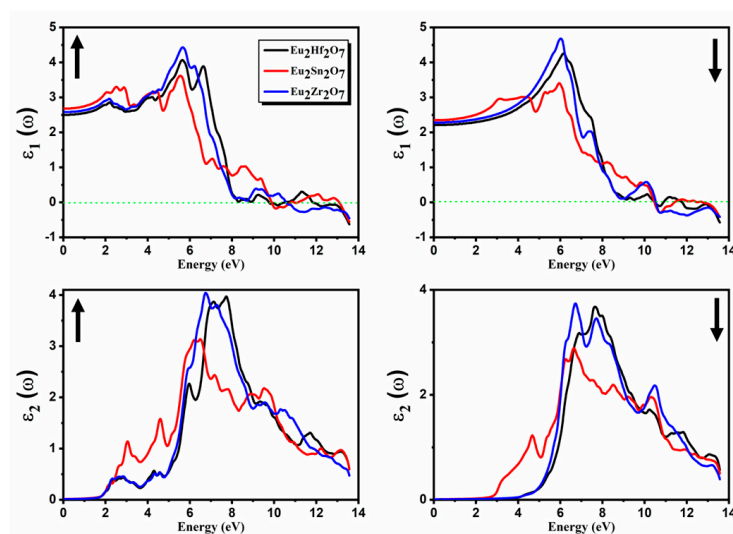
Figure 6. Calculated $\varepsilon_1(\omega)$ and $\varepsilon_2(\omega)$ plots for $Eu_2Tm_2O_7$ (Tm = Hf, Sn, Zr).

Calculated values of $\varepsilon_1(0)$ in the spin up channel are approximately 2,48, 2.53 and 2.61 for $Eu_2Hf_2O_7$, $Eu_2Sn_2O_7$ and $Eu_2Zr_2O_7$, respectively. However, calculated values of

the $\varepsilon_1(0)$ for the spin down channel are approximately 2.11, 2.13 and 2.15 for $Eu_2Hf_2O_7$, $Eu_2Sn_2O_7$ and $Eu_2Zr_2O_7$, respectively.

An important parameter that explains the optical transitions between VB and CB is known as the imaginary part $\varepsilon_2(\omega)$ of the dielectric function. The calculated spectra of $\varepsilon_2(\omega)$ for $Eu_2Tm_2O_7$ (Tm = Hf, Sn, Zr) using the GGA+U approximation are shown in Figure 6. Notable peaks in the visible region are due to the presence of an intermediate band in the spin up channel. In both spin channels, significant absorption of the incoming photons is also shown by these compounds in the UV region. Maximum values of $\varepsilon_2(\omega)$ occur around 6.0 eV for all compounds and in both spin channels. Inter-band transitions between the VB and CB are responsible for these points. The selection rule states that the allowed transitions are only those having change in the angular momentum $\Delta l = \pm 1$. From Figure 6, it is evident that initially, there is no peak in $\varepsilon_2(\omega)$ plots and originates from some finite energy values known as threshold energies. In the spin up channel, the values of the threshold energy for $\varepsilon_2(\omega)$ are 1.8 eV for $Eu_2Tm_2O_7$ (Tm = Hf, Sn, Zr). However, for the spin down channel, the threshold values of $\varepsilon_2(\omega)$ are 3.97, 2.78 and 3.98 for $Eu_2Hf_2O_7$, $Eu_2Sn_2O_7$ and $Eu_2Zr_2O_7$, respectively. These compounds are potential candidates for photovoltaic applications such as solar cells due to efficient absorption of incoming photons in visible and UV regions.

Calculated values of the $\varepsilon_1(\omega)$ and $\varepsilon_2(\omega)$ are used to calculate other optical parameters such as the absorption coefficient $\alpha(\omega)$, real optical conductivity $\sigma(\omega)$, refractive index $n(\omega)$, extinction coefficient $K(\omega)$, reflectivity $R(\omega)$ and energy loss function $L(\omega)$. Deep knowledge of these optical parameters is required while designing efficient optical devices, i.e., ultraviolet (UV) photodetectors, semiconductor lasers and optically transparent electrodes. The following equations are used to calculate the aforementioned optical parameters [37]:

$$\widetilde{n}(\omega) = n(\omega) + ik(\omega) \tag{6}$$

$$n(\omega) = 1 + \frac{2}{\pi} P \int_0^\infty \frac{k(\omega')}{\omega' - \omega} d\omega' \tag{7}$$

$$k(\omega) = -\frac{2}{\pi} P \int_0^\infty \frac{n(\omega') - 1}{\omega' - \omega} d\omega' \tag{8}$$

$$n(\omega) = \left[\frac{\sqrt{(\varepsilon_1^2 \omega) + \varepsilon_2^2(\omega)}}{2} + \frac{\varepsilon_1(\omega)}{2} \right]^{\frac{1}{2}} \tag{9}$$

$$k(\omega) = \left[\frac{\sqrt{\varepsilon_1^2(\omega) + \varepsilon_2^2(\omega)}}{2} + \frac{\varepsilon_1(\omega)}{2} \right]^{\frac{1}{2}} \tag{10}$$

$$n(0) = \sqrt{\varepsilon_1(0)} \tag{11}$$

$$R(\omega) = \left| \frac{\widetilde{n}(\omega) - 1}{\widetilde{n}(\omega) + 1} \right| = \frac{(1 + n)^2 + k^2}{(1 - n)^2 + k^2} \tag{12}$$

$$\sigma(\omega) = \frac{\omega}{4\pi} \varepsilon_2(\omega) \tag{13}$$

$$\alpha(\omega) = \sqrt{2\omega} \left[\sqrt{\varepsilon_1^2(\omega) + \varepsilon_2^2(\omega)} - \varepsilon_1(\omega) \right]^{\frac{1}{2}} \tag{14}$$

$$k(\omega) = \frac{c}{2\omega} \alpha(\omega) \tag{15}$$

$$L(\omega) = -Im\left(\frac{1}{\varepsilon(\omega)}\right) = \frac{\varepsilon_2(\omega)}{\varepsilon_1^2(\omega) + \varepsilon_2^2(\omega)} \tag{16}$$

Handsome knowledge of $n(\omega)$ is essential before opting an optical material for technological device applications. A potential photovoltaic compound must have some fundamental properties such as high optical conductivity, high absorption coefficient, low emissivity and high refractive index. The calculated spectra of $n(\omega)$ for $Eu_2Tm_2O_7$ (Tm = Hf, Sn, Zr) using the GGA+U approximation are shown in the Figure 7. The major peaks around 6.0 eV in the spectra of $n(\omega)$ after static values show that the maximum dispersion of the incoming photons by these materials occurs at this value. We can spot in the spectra of $n(\omega)$ for the spin up channel that the curves of $Eu_2Tm_2O_7$ (Tm = Hf, Sn, Zr) become less than unity at approximately 9.0 eV. Similarly, we can spot in the spectra of $n(\omega)$ for the spin down channel that the curves of $Eu_2Tm_2O_7$ (Tm = Hf, Sn, Zr) become less than unity at approximately 10.0 eV. Values of the $n(\omega)$ at zero frequency ($\omega = 0$) are known as static values of refractive index $n(0)$. The values of $n(0)$ and E_g are related with each other using Equation (17) [38]:

$$n(0) = \sqrt{1 + \left(\frac{h\omega_p}{E_g}\right)} \tag{17}$$
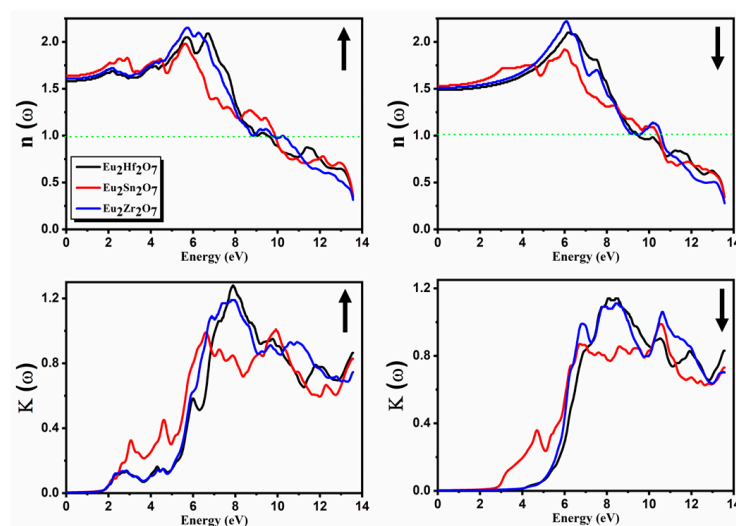
Figure 7. Calculated $n(\omega)$ and $K(\omega)$ plots for $Eu_2Tm_2O_7$ (Tm = Hf, Sn, Zr).

Calculated values of $n(0)$ for the spin up channel are 1.53, 1.57 and 1.61 for $Eu_2Hf_2O_7$, $Eu_2Sn_2O_7$ and $Eu_2Zr_2O_7$, respectively. However, calculated values of the $n(0)$ for the spin down channel are 1.49, 1.49 and 1.52 for $Eu_2Hf_2O_7$, $Eu_2Sn_2O_7$ and $Eu_2Zr_2O_7$, respectively.

The calculated spectra of $K(\omega)$ for $Eu_2Tm_2O_7$ (Tm = Hf, Sn, Zr) using the GGA+U approximation are shown in Figure 7. We can note that $\varepsilon_2(\omega)$ and $K(\omega)$ have an analogous profile. Notable peaks in the visible region are due to the presence of an intermediate band in the spin up channel. In both spin channels, significant absorption of the incoming photons is also shown by these compounds in the UV region. Maximum values of $K(\omega)$ occur around 8.0 eV for all compounds and in both spin channels. From Figure 6, it is evident that initially there is no peak in $K(\omega)$ plots and originates from some finite energy values known as threshold energies. In the spin up channel, the values of the threshold energy for $K(\omega)$ is 1.9 eV for $Eu_2Tm_2O_7$ (Tm = Hf, Sn, Zr). However, threshold values of $K(\omega)$ are 3.97, 2.78 and 3.98 for $Eu_2Hf_2O_7$, $Eu_2Sn_2O_7$ and $Eu_2Zr_2O_7$, respectively. We can conclude on the basis of these results that the compounds under study are potential candidates for photovoltaic applications such as solar cells due to efficient absorption of incoming photons in the visible region.

The ratio of reflected to incident photons for a material is known as reflectivity $R(\omega)$. The calculated spectra of $R(\omega)$ for $Eu_2Tm_2O_7$ (Tm = Hf, Sn, Zr) using the GGA+U approximation are shown in Figure 8. It is evident from Figure 8 that these materials are weak reflectors of incident photons, as they reflect approximately 25% of incident photons from 0 to 12 eV. Values of the $R(\omega)$ at zero frequency ($\omega = 0$) are known as static values of reflectivity $R(0)$. Calculated values of $R(0)$ for the spin up channel are 0.050, 0.052 and 0.058 for $Eu_2Hf_2O_7$, $Eu_2Sn_2O_7$ and $Eu_2Zr_2O_7$, respectively. However, calculated values of the $R(0)$ for the spin down channel are 0.041, 0.43 and 0.49 for $Eu_2Hf_2O_7$, $Eu_2Sn_2O_7$ and $Eu_2Zr_2O_7$, respectively. We can conclude on the basis of these results that these compounds can be utilized in applications such as anti-reflecting coatings.
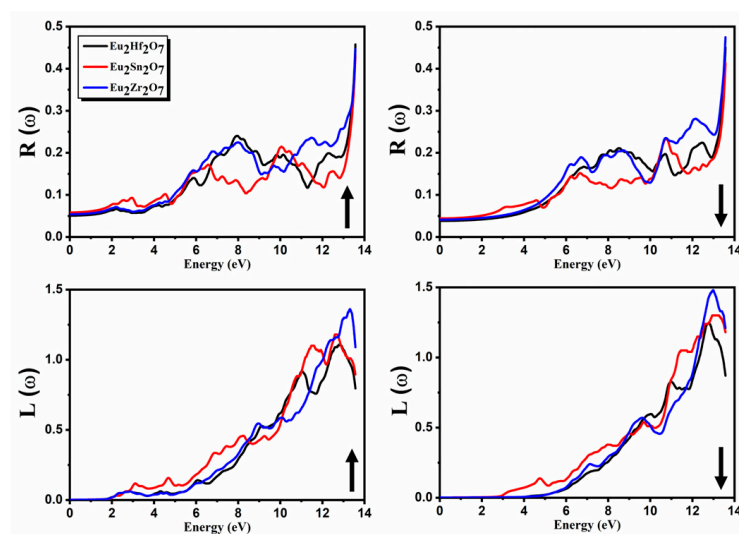
Figure 8. Calculated $R(\omega)$ and $L(\omega)$ plots for $Eu_2Tm_2O_7$ (Tm = Hf, Sn, Zr).

Energy loss function $L(\omega)$ plays an important role while investigating optical properties of the materials. The entire energy range is covered by $L(\omega)$, consisting of elastically scattered and non-scattered electrons that are responsible for electronic transitions between VB and CB. Energy lost by the electrons passing through the material with sufficient energy is described by $L(\omega)$. Inter-band transitions are responsible for the major peaks in the spectra of $L(\omega)$. The calculated spectra of $L(\omega)$ for $Eu_2Tm_2O_7$ (Tm = Hf, Sn, Zr) using the GGA+U approximation are shown in Figure 8. The major peaks specify the values of plasmon resonance, and major peaks in the spectra of $L(\omega)$ occur at approximately 13.1, 12.7 and 13.2 eV for $Eu_2Hf_2O_7$, $Eu_2Sn_2O_7$ and $Eu_2Zr_2O_7$, respectively, for the spin up channel. However, for the spin down channel, major peaks occur at approximately 12.8, 13.1 and 12.9 eV for $Eu_2Hf_2O_7$, $Eu_2Sn_2O_7$ and $Eu_2Zr_2O_7$, respectively.

The calculated spectra of real optical conductivity $\sigma(\omega)$ for $Eu_2Tm_2O_7$ (Tm = Hf, Sn, Zr) using the GGA+U approximation are shown in the Figure 9. Notable peaks in the visible region are due to the presence of an intermediate band in the spin up channel. In both spin channels, significant absorption of the incoming photons is also shown by these compounds in the UV region. Maximum values of $\sigma(\omega)$ occur around 7.0 eV for all compounds and in both spin channels. From Figure 9, it is evident that initially, there is no peak in $\sigma(\omega)$ plots and originates from some finite energy values known as threshold energies. In the spin up channel, the values of the threshold energy for $\sigma(\omega)$ are 1.9 eV for $Eu_2Tm_2O_7$ (Tm = Hf, Sn, Zr). However, threshold values of $\sigma(\omega)$ are 2.0, 2.88 and 3.2 for $Eu_2Hf_2O_7$, $Eu_2Sn_2O_7$ and $Eu_2Zr_2O_7$, respectively. It is a well-known fact that excitations will be produced when photon energy is greater than E_g. We can conclude on the basis of these results that the compounds under study are potential candidates for photovoltaic applications such as solar cells due to efficient absorption of incoming photons in the visible and UV regions.
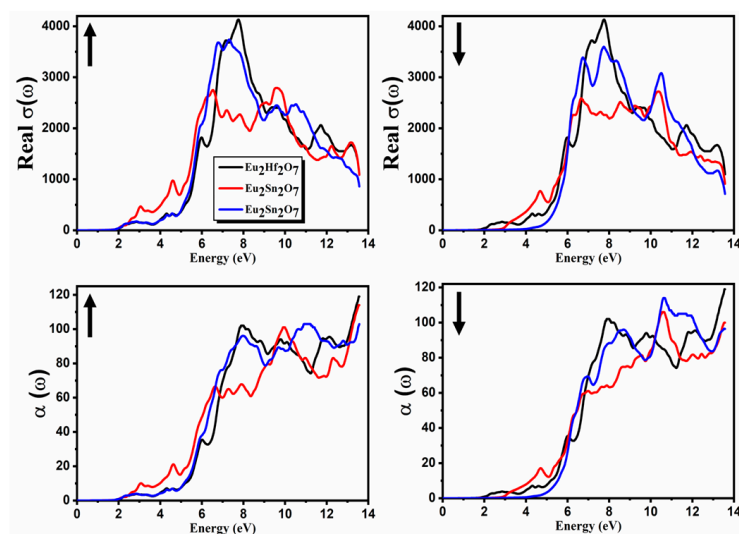
Figure 9. Calculated $\sigma(\omega)$ and $\alpha(\omega)$ plots for Eu$_2$Tm$_2$O$_7$ (Tm = Hf, Sn, Zr).

3. Materials and Methods

The electronic, optical and magnetic properties of pyrochlore oxides Eu$_2$Tm$_2$O$_7$ (Tm = Hf, Sn, Zr) are calculated within the framework of DFT using the generalized gradient approximation (GGA), taking into account the effect of the Hubbard potential (GGA+U) as implemented in Wein2k [38]. An exceedingly precise, full potential linearized augmented plane wave (FP-LAPW) technique [39] was used for the calculations of optical and electronic properties of Eu$_2$Tm$_2$O$_7$ (Tm = Hf, Sn, Zr). Relaxed structures were used to calculate ground state properties of the aforementioned compounds. The unit cell was divided into two regions while working with the FP-LAPW technique: (a) atomic Sphere (Muffin-tin) and (b) interstitial region (IR).

Cut-off values for the plane wave basis set were assumed to be $R_{MT} \times K_{MAX} = 7.0$ (R_{MT} is smallest muffin-tin radius and K_{MAX} is maximum length of fermi wave vector, respectively). The value of l_{MAX} equal to 10 (angular momentum with maximum length) was taken to expand the wave function. Forces on the atoms in the unit cell were minimized up to 10^{-3} $Ry/a.u$ to obtain relaxed geometry. Self-consistent field calculations were terminated when forces on atoms became less than 10^{-3} $Ry/a.u.$ The value of -6.0 Ry was taken to ensure no leakage of charge from the core state. The crystalline structures for Eu$_2$Tm$_2$O$_7$ (Tm = Hf, Sn, Zr) are shown in Figure 10.
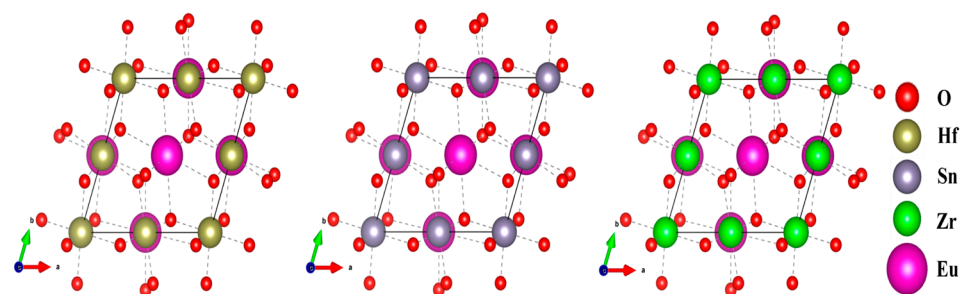
Figure 10. Crystalline structure for Eu$_2$Tm$_2$O$_7$ (Tm = Hf, Sn, Zr).

4. Conclusions

The electronic, optical and magnetic properties of Eu$_2$Tm$_2$O$_7$ (Tm = Hf, Sn, Zr) were investigated using FP-LAPW-based ab-initio calculations. Band structure plots reveal that these compounds are direct bandgap semiconductors. The presence of the intermediate band in the spin up channel plays a vital role in electronic transitions between VB and CB. To obtain insight into the active involvement of various atoms and electronic states

in the electronic transitions of these materials, partial/total densities of states were also examined. The shape and height of the curves were different for the spin up and spin down channels in the TDOS spectrum, which shows that these compounds have strong magnetic properties. $Eu_2Tm_2O_7$ (Tm = Hf, Sn, Zr) possess nearly the same values of magnetic moments. We discovered that band structures and DOS support the computed optical properties. Based on the calculated $n(\omega)$, we can say that $Eu_2Tm_2O_7$ (Tm = Hf, Sn, Zr) are optically active compounds, as their refractive index is between 1.0 to 2.0. It is concluded based on $R(\omega)$ results that these compounds are very weak reflectors of incident photons. These compounds reflect approximately 25% of the incident photons. The optical conductivity $\sigma(\omega)$ shows that these materials absorb the maximum of the incident photons in visible and UV regions. These compounds are promising candidates for potential optoelectronic applications such as solar cells working in visible and UV regions.

Author Contributions: Conceptualization, methodology J.J.; writing—review and editing, supervision S.H.; writing—original draft, A.N.; software, data curation, Z.A.; formal analysis, writing—review and editing, S.M.; validation, resources, H.A.; formal analysis, writing—review and editing, A.A. All authors have read and agreed to the published version of the manuscript.

Funding: This research was supported by Basic Science Research Program through the National Research Foundation of Korea (NRF) funded by the Ministry of Education (2020R1A6A1A03043435, 2022R1F1A1074324). This research was also funded by RGP2/272/44.

Data Availability Statement: Not applicable.

Acknowledgments: The authors extend their appreciation to the Deanship of Scientific Research at King Khalid University for funding the work through the research project under grant number RGP2/272/44.

Conflicts of Interest: The authors declare no conflict of interest.

References

1. Shannon, R.; Sleight, A. Synthesis of new high-pressure pyrochlore phases. *Inorg. Chem.* **1968**, *7*, 1649–1651. [CrossRef]
2. Fu-k'ang, F.; Kuznetsov, A.; Keler, É. Zirconates of the rare earth elements and their physicochemical properties. Report 1. Zirconates of lanthanum, neodymium and cerium. *Bull. Acad. Sci. USSR Div. Chem. Sci.* **1964**, *13*, 1070–1075. [CrossRef]
3. Kostov, I. *Mineralogy*; Oliver and Boyd Ltd.: Edinburgh/London, UK, 1968.
4. Shamblin, J.; Feygenson, M.; Neuefeind, J.; Tracy, C.L.; Zhang, F.; Finkeldei, S.; Bosbach, D.; Zhou, H.; Ewing, R.C.; Lang, M. Probing disorder in isometric pyrochlore and related complex oxides. *Nat. Mater.* **2016**, *15*, 507–511. [CrossRef] [PubMed]
5. Lin, L.; Guo, Y.; Gillen, R.; Robertson, J. Chemical trends of defects at HfO_2: GaAs and Al_2O_3: GaAs/InAs/InP/GaSb interfaces. *J. Appl. Phys.* **2013**, *113*, 134103. [CrossRef]
6. Liu, D.; Lin, L.; Liu, M.; Yan, Z.; Dong, S.; Liu, J.-M. Multiferroicity in spin ice $Ho_2Ti_2O_7$: An investigation on single crystals. *J. Appl. Phys.* **2013**, *113*, 17D901. [CrossRef]
7. Yan, H.; Ning, H.; Kan, Y.; Wang, P.; Reece, M.J. Piezoelectric ceramics with super-high curie points. *J. Am. Ceram. Soc.* **2009**, *92*, 2270–2275. [CrossRef]
8. Lee, S.; Park, J.-G.; Adroja, D.; Khomskii, D.; Streltsov, S.; McEwen, K.; Sakai, H.; Yoshimura, K.; Anisimov, V.; Mori, D. Spin gap in $Tl_2Ru_2O_7$ and the possible formation of Haldane chains in three-dimensional crystals. *Nat. Mater.* **2006**, *5*, 471–476. [CrossRef]
9. Trojan-Piegza, J.; Zych, E.; Kosińska, M. Fabrication and spectroscopic properties of nanocrystalline $La_2Hf_2O_7$: Pr. *Radiat. Meas.* **2010**, *45*, 432–434. [CrossRef]
10. Zhang, A.; Lü, M.; Yang, Z.; Zhou, G.; Zhou, Y. Systematic research on $RE_2Zr_2O_7$ (RE = La, Nd, Eu and Y) nanocrystals: Preparation, structure and photoluminescence characterization. *Solid State Sci.* **2008**, *10*, 74–81. [CrossRef]
11. Zhang, J.; Lian, J.; Fuentes, A.F.; Zhang, F.; Lang, M.; Lu, F.; Ewing, R.C. Enhanced radiation resistance of nanocrystalline pyrochlore $Gd_2(Ti_{0.65}Zr_{0.35})_2O_7$. *Appl. Phys. Lett.* **2009**, *94*, 243110. [CrossRef]
12. Shimizu, Y.; Nishi, H.; Suzuki, H.; Maeda, K. Solid-state NOx sensor combined with NASICON and Pb–Ru-based pyrochlore-type oxide electrode. *Sens. Actuators B Chem.* **2000**, *65*, 141–143. [CrossRef]
13. Li, Y.J.; Tsai, P.P. Lacunar pyrochlore-type tungsten oxides as humidity-sensing materials. *Solid State Ion.* **1996**, *86*, 1001–1004. [CrossRef]
14. Yang, J.; Han, Y.; Shahid, M.; Pan, W.; Zhao, M.; Wu, W.; Wan, C. A promising material for thermal barrier coating: Pyrochlore-related compound Sm_2FeTaO_7. *Scr. Mater.* **2018**, *149*, 49–52. [CrossRef]
15. Rekhila, G.; Brahimi, R.; Bessekhouad, Y.; Trari, M. Physical and photoelectrochemical characterizations of the pyrochlore $La_{1.9}Ba_{0.1}Sn_2O_7$: Application to chromate reduction under solar light. *J. Photochem. Photobiol. A Chem.* **2017**, *332*, 345–350. [CrossRef]

16. Uno, W.; Fujii, K.; Niwa, E.; Torii, S.; Miao, P.; Kamiyama, T.; Yashima, M. Experimental visualization of oxide-ion diffusion paths in pyrochlore-type $Yb_2Ti_2O_7$. *J. Ceram. Soc. Jpn.* **2018**, *126*, 341–345. [CrossRef]

17. Chakoumakos, B.C. Systematics of the pyrochlore structure type, ideal $A_2B_2X_6Y$. *J. Solid State Chem.* **1984**, *53*, 120–129. [CrossRef]

18. Subramanian, M.A.; Aravamudan, G.; Subba Rao, G.V. Oxide pyrochlores—A review. *Prog. Solid State Chem.* **1983**, *15*, 55–143. [CrossRef]

19. Zhang, B.; Dewasurendra, S.; Zhang, F. Blue and red up-conversion light emission in TM-doped $A_2B_2O_7$ oxides. *Mater. Lett.* **2016**, *170*, 53–57. [CrossRef]

20. Lang, M.; Zhang, F.; Zhang, J.; Wang, J.; Lian, J.; Weber, W.; Schuster, B.; Trautmann, C.; Neumann, E.; Ewing, R. Review of $A_2B_2O_7$ pyrochlore response to irradiation and pressure. *Nucl. Inst. Methods Phys. Res. B Elsevier BV* **2010**, *268*, 2951–2959. [CrossRef]

21. Zhang, F.; Lang, M.; Ewing, R. Atomic disorder in $Gd_2Zr_2O_7$ pyrochlore. *Appl. Phys. Lett.* **2015**, *106*, 191902. [CrossRef]

22. Kramer, S.; Tuller, H. A novel titanate-based oxygen ion conductor: $Gd_2Zr_2O_7$. *Solid State Ion.* **1995**, *82*, 15–23. [CrossRef]

23. Aguilar, T.; Navas, J.; De los Santos, D.M.; Sánchez-Coronilla, A.; Fernández-Lorenzo, C.; Alcántara, R.; Gallardo, J.J.; Blanco, G.; Martín-Calleja, J. TiO2 and pyrochlore $Tm_2Ti_2O_7$ based semiconductor as a photoelectrode for dye-sensitized solar cells. *J. Phys. D Appl. Phys.* **2015**, *48*, 145102. [CrossRef]

24. Ullah, N.; Ali, Z.; Khan, I.; Rehman, G.; Ahmad, I. Structural, Mechanical and Optoelectronic Properties of $Y_2M_2O_7$ (M = Ti, V and Nb) Pyrochlores: A First Principles Study. *J. Electron. Mater.* **2017**, *46*, 4640–4648. [CrossRef]

25. Li, X.; Cai, Y.; Cui, Q.; Lin, C.; Dun, Z.; Matsubayashi, K.; Uwatoko, Y.; Sato, Y.; Kawae, T.; Lv, S. Long-range magnetic order in the Heisenberg pyrochlore antiferromagnets $Gd_2Ge_2O_7$ and $Gd_2Pt_2O_7$ synthesized under high pressure. *Phys. Rev. B* **2016**, *94*, 214429. [CrossRef]

26. Hallas, A.; Sharma, A.; Cai, Y.; Munsie, T.; Wilson, M.; Tachibana, M.; Wiebe, C.; Luke, G. Relief of frustration in the Heisenberg pyrochlore antiferromagnet $Gd_2Pt_2O_7$. *Phys. Rev. B* **2016**, *94*, 134417. [CrossRef]

27. Jacob, K.T.; Lwin, K.T.; Waseda, Y. System La-Pd-O: Phase diagram and thermodynamic properties of ternary oxides. *Solid State Sci.* **2002**, *4*, 205–215. [CrossRef]

28. Duran, R.R.; Falsetti, P.E.; Muhr, L.; Privat, R.; Barth, D. Phase equilibrium study of the ternary system $CO_2 + H_2O$ + ethanol at elevated pressure: Thermodynamic model selection. Application to supercritical extraction of polar compounds. *J. Supercrit. Fluids* **2018**, *138*, 17–28. [CrossRef]

29. Child, M.; Koskinen, O.; Linnanen, L.; Breyer, C. Sustainability guardrails for energy scenarios of the global energy transition. *Renew. Sustain. Energy Rev.* **2018**, *91*, 321–334. [CrossRef]

30. Shibasaki, S.; Terasaki, I. Thermoelectric Properties of Layered Pd Oxide R_2PdO_4 (R = La, Nd, Sm, and Gd). *J. Phys. Soc. Jpn.* **2006**, *75*, 024705. [CrossRef]

31. Attfield, J.P.; Férey, G. Structural correlations within the lanthanum palladium oxide family. *J. Solid State Chem.* **1989**, *80*, 286–298. [CrossRef]

32. Yang, J.; Zhou, J.; Huang, Y.; Tong, Y. Lanthanide-Based Dual Modulation in Hematite Nanospindles for Enhancing the Photocatalytic Performance. *ACS Appl. Nano Mater.* **2022**, *5*, 8557–8565. [CrossRef]

33. Zhang, J.; Huang, Y.; Lu, X.; Yang, J.; Tong, Y. Enhanced BiVO4 photoanode photoelectrochemical performance via borate treatment and a NiFeOx cocatalyst. *ACS Sustain. Chem. Eng.* **2021**, *9*, 8306–8314. [CrossRef]

34. Azam, S.; Abbas, Z.; Gul, B.; Khan, M.S.; Irfan, M.; Sohail, M.; Khan, S.A.; Naseer, F.; Irfan, A.; Khan, G. First-principles calculations of optoelectronic properties of CaO: Eu^{+2} (SrO: Eu^{+2}) for energy applications. *Int. J. Mod. Phys. B* **2018**, *32*, 1850333. [CrossRef]

35. Abbas, Z.; Fatima, K.; Muhammad, S.; Siddeeg, S.M.; Ali, A.; Hussain, S.; Jung, J. Investigating the effect of alkali metals on the structural & optoelectronic properties of hexafluorozirconate red phosphors A_2ZrF_6 (A = Cs, K, Na) using first-principles calculations: A prospect for warm-white LEDs (w-LEDs) applications. *J. Solid State Chem.* **2023**, *317*, 123689.

36. Abbas, Z.; Fatima, K.; Gorczyca, I.; Jaffery, S.H.A.; Ali, A.; Irfan, M.; Raza, H.H.; Algarni, H.; Muhammad, S.; Teisseyre, H. First-principles calculations to investigate electronic, optical, and thermoelectric properties of Na_2GeX_3 (X = S, Se, Te) for energy applications. *Mater. Sci. Semicond. Process.* **2023**, *154*, 107206. [CrossRef]

37. Fatima, K.; Abbas, Z.; Naz, A.; Alshahrani, T.; Chaib, Y.; Jaffery, S.H.A.; Muhammad, S.; Hussain, S.; Jung, J.; Algarni, H. Shedding light on the structural, optoelectronic, and thermoelectric properties of pyrochlore oxides ($La_2Q_2O_7$ (Q = Ge, Sn)) for energy applications: A first-principles investigation. *J. Solid State Chem.* **2022**, *313*, 123305. [CrossRef]

38. Abbas, Z.; Hussain, S.; Muhammad, S.; Siddeeg, S.M.; Jung, J. A First-Principles Investigation on the Structural, Optoelectronic, and Thermoelectric Properties of Pyrochlore Oxides ($La_2Tm_2O_7$ (Tm = Hf, Zr)) for Energy Applications. *Int. J. Mol. Sci.* **2022**, *23*, 15266. [CrossRef]

39. Abbas, Z.; Fatima, K.; Jaffery, S.H.A.; Ali, A.; Raza, H.H.; Muhammad, S.; Algarni, H.; Hussain, S.; Jung, J. Ab-initio study of Nb-based complex materials: A new class of materials for optoelectronic applications. *J. Comput. Sci.* **2022**, *63*, 101791. [CrossRef]